

# Observation of topological transitions associated with a Weyl exceptional ring

Hao-Long Zhang,<sup>1,\*</sup> Pei-Rong Han,<sup>1,\*</sup> Xue-Jia Yu,<sup>1,\*</sup> Shou-Bang Yang,<sup>1</sup> Jia-Hao Lü,<sup>1</sup> Wen Ning,<sup>1,†</sup> Fan Wu,<sup>1</sup> Qi-Ping Su,<sup>2</sup> Chui-Ping Yang,<sup>2</sup> Zhen-Biao Yang,<sup>1,3,‡</sup> and Shi-Biao Zheng<sup>1,3,§</sup>

<sup>1</sup>*Fujian Key Laboratory of Quantum Information and Quantum Optics,  
College of Physics and Information Engineering, Fuzhou University, Fuzhou 350108, China*

<sup>2</sup>*School of Physics, Hangzhou Normal University, Hangzhou 311121, China*

<sup>3</sup>*Hefei National Laboratory, Hefei 230088, China*

The environment-induced dissipation of an open system, once thought as a nuisance, can actually lead to emergence of many intriguing phenomena that are absent in an isolated system. Among these, Weyl exceptional rings (WER), extended from point-like singularities, are particularly interesting. Theoretically, a WER was predicted to carry a topological charge with a nonzero Chern number, but it has not been measured so far. We here investigate this topology in a circuit, where the WER is synthesized with a superconducting qubit controllably coupled to a decaying resonator. The high flexibility of the system enables us to characterize its eigenvectors on different manifolds of parameter space. We extract both the quantized Berry phase and Chern number from these eigenvectors. Furthermore, we demonstrate a topological transition triggered by shrinking the size of the manifold—a unique feature of the WER.

## I. INTRODUCTION

Weyl Fermions refer to massless particles that satisfy the Weyl equation, first predicted by Hermann Weyl in 1929 [1]. Neutrinos were once thought to be Weyl Fermions until the discovery of their oscillations [2], implying they possess very tiny but nonzero masses. Although such exotic particles have not been found in nature as elementary particles even after a long-time exploration, a quasi-particle that behaves like a Weyl particle can emerge in some topological materials. One of such examples is the Weyl semimetals [3–6], where two linear dispersion bands cross at a single degenerate point in three-dimensional momentum space. Such a point is referred to as the Weyl point, near which the system dynamics is mathematically governed by the Weyl equation featuring spin-orbit coupling. The Weyl point is the analog of a magnetic monopole [7], which carries a topological charge that emanates a Berry flux [8]. Due to the presence of the topological defect, a region enclosing it displays a nontrivial doubly-connected topological structure [9], with the global geometric feature quantified by a quantized Chern number.

When a non-Hermitian (NH) dynamics is added to the Weyl Hamiltonian, a point-like node can be transformed into a ring-like structure of exceptional points (EPs) referred to as the WER [10–13], along which both the eigenenergies and eigenvectors coalesce [14–17]. The WER can display topological features that are inaccessible with isolated EPs. One of such intriguing features is the presence of a nonzero quantized Chern number, as a consequence of the quantized Berry flux piercing

through the surface that encloses the whole ring. On the contrary, when the ring is outside the manifold, no Berry charge is enclosed; thus, the Chern number is zero. This striking feature implies that the topological charge is preserved under an NH perturbation, which spreads the point-like charge over a ring. This fundamentally changes the topological structure of the parameter space where the topological charge resides, enabling the occurrence of a topological transition that cannot occur with a point-like topological defect. So far, WERs have been observed in classical wave systems [18–24], but a quantum version has not been realized, though isolated EPs have been observed in spin-boson systems [25, 26]. Even for the classical implementations, the nontrivial topological feature of the manifold enclosing the WER—characterized by a nonzero Chern number—has not been observed so far.

We here investigate the topological transition associated with the WER encoded in the entangled eigenvectors of a dissipative Jaynes-Cummings (JC) model. This model consists of a qubit and a decaying resonator, engineered with a circuit quantum electrodynamics (QED) architecture. One of the superconducting qubits in the circuit QED device is coupled to its readout resonator with an ac flux that produces a longitudinal parametric modulation to the qubit’s transition frequency. The effective qubit-resonator coupling strength and detuning are tunable by the modulation amplitude and frequency. In the absence of dissipation, the Berry topological charge is carried by the degeneracy of the qubit-boson entangled eigenstates, which resides at the origin of the parameter space. The dissipation extends the point-like singularity to a ring, realizing a WER in the parameter space. The Berry curvature, which serves as a fictitious magnetic field, is extracted from the eigenvectors measured for different settings of the control parameter. By reducing the size of the manifold so as not to enclose the WER, the system undergoes a topological transition, manifested by an abrupt change of the Berry phase and the Chern

\* These authors contribute equally to this work.

† ningw@fzu.edu.cn

‡ zbyang@fzu.edu.cn

§ t96034@fzu.edu.cn

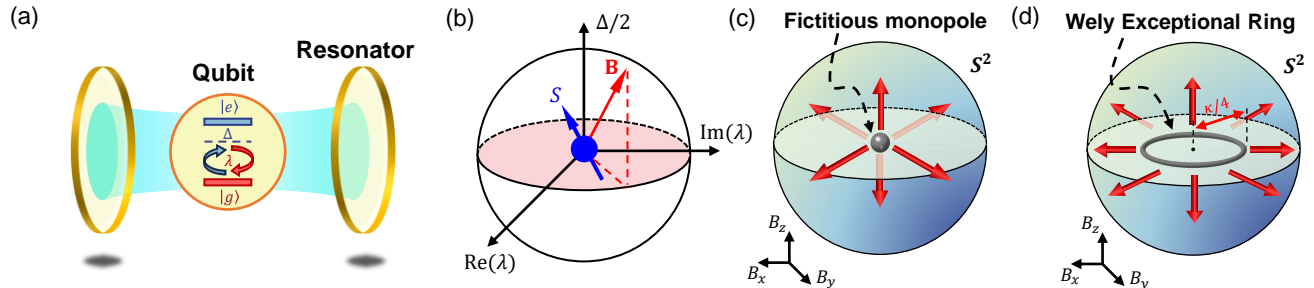


FIG. 1. Construction of the WER. (a) The JC model. The system is composed of a photonic mode stored in a resonator interacting with a qubit, whose upper and lower levels are respectively denoted as  $|e\rangle$  and  $|g\rangle$ . The qubit-resonator coupling coefficient and detuning are  $\lambda$  and  $\Delta$ , respectively. (b) Spin representation. In the single-excitation subspace  $\{|\uparrow\rangle \equiv |e, 0\rangle, |\downarrow\rangle \equiv |g, 1\rangle\}$ , the dynamics of the composite system is mathematically equivalent to a spin-1/2 ( $S$ ) moving in a magnetic field  $\mathbf{B}$ , whose  $x$ -,  $y$ -, and  $z$ -components correspond to  $\text{Re}(\lambda)$ ,  $\text{Im}(\lambda)$ , and  $\Delta/2$ , respectively. (c) Point-like topological defect. In the absence of dissipation, the eigenspectrum displays a two-fold degeneracy at the origin of the 3D parameter space  $\{B_x, B_y, B_z\}$ , which can be considered as a fictitious monopole carrying a quantized topological charge. (d) WER. The non-Hermiticity is manifested by the photonic dissipation of the resonator with a rate  $\kappa$ . Due to the presence of dissipation, the point-like singularity is extended to a ring with the radius of  $B_{WER} = \kappa/4$ , centered at the origin and located on the  $xy$ -plane of the parameter space.

number.

## II. MODEL SYSTEM

We first consider the topology encoded in the parameter space of the JC model without dissipation [Fig. 1(a)]. In the framework rotating at the frequency of the resonator, the system Hamiltonian is given by (setting  $\hbar = 1$ )

$$H_S = \Delta |e\rangle \langle e| + \lambda a^\dagger |g\rangle \langle e| + \lambda^* a |e\rangle \langle g|, \quad (1)$$

where  $|e\rangle$  and  $|g\rangle$  are the upper and lower levels of the qubit,  $a^\dagger$  and  $a$  are the creation and annihilation operators for the quantized field stored in the resonator, and  $\lambda$  and  $\Delta$  denote the qubit-cavity coupling coefficient and detuning, respectively. In the single-excitation subspace, the composite qubit-resonator system can be taken as a spin, with the basis states  $|e, 0\rangle$  and  $|g, 1\rangle$  respectively corresponding to the spin-up and -down states  $|\uparrow\rangle$  and  $|\downarrow\rangle$ , where the number in each ket denotes the photon number of the resonator. With this analogy, the system dynamics can be described as the motion of the spin in a magnetic field  $\mathbf{B}$  with the components  $B_x = \text{Re}(\lambda)$ ,  $B_y = \text{Im}(\lambda)$ , and  $B_z = \Delta/2$ , as shown in Fig 1(b). This Hermitian system has a degeneracy at the origin, referred to as a diabolic point, where the two eigenenergies coalesce but the eigenvectors do not. This degeneracy is a mathematic analog of the magnetic monopole that carries a quantized topological charge in the parameter space, as shown in Fig. 1(c). Due to the presence of such a topological defect, any manifold that encloses this singularity in the parameter space is topologically distinct from those without involving it. The fictitious magnetic field emanated from the topological charge is manifested by the Berry curvature. The quantized Berry flux penetrating

through the manifold is characterized by the Chern number, defined as the integral of the Berry curvature over the manifold.

With the dissipation of the photonic field being included, the system dynamics is described by a master equation. Conditional upon no photon being leaked into the environment, the system dynamics is described by the NH Hamiltonian

$$H_{NH} = H_S - \frac{1}{2} i\kappa a^\dagger a, \quad (2)$$

with  $\kappa$  being the decaying rate of the photonic field. The eigenvectors of the NH Hamiltonian are drastically different from those of its Hermitian counterpart. Due to the non-Hermiticity, the left and right eigenvectors, defined as  $H_{NH} |u_n^r\rangle = E_n |u_n^r\rangle$  and  $\langle u_n^l | H_{NH} = \langle u_n^l | E_n$ , are not the Hermitian conjugates of each other, and need to be obtained separately. For the present NH Hamiltonian, the two non-orthogonal right eigenvectors,  $|u_n^r\rangle$  ( $n = 1, 2$ ), in the single-excitation subspace can be written as

$$|u_n^r\rangle = \frac{\lambda^* |e, 0\rangle + (E_n - \Delta) |g, 1\rangle}{\sqrt{|\lambda|^2 + |E_n - \Delta|^2}}, \quad (3)$$

where

$$E_{1,2} = \frac{2\Delta - i\kappa}{4} \pm \sqrt{|\lambda|^2 + \frac{(2\Delta + i\kappa)^2}{16}}. \quad (4)$$

The left eigenvectors can be obtained from the biorthonormal condition

$$\langle u_n^l | u_m^r \rangle = \delta_{m,n}. \quad (5)$$

The non-Hermiticity changes the point-like degeneracy into a WER with the radius of  $B_{WER} = \kappa/4$ , centered

at the origin and located on the  $B_x$ - $B_y$  plane of the parameter space [Fig. 1(d)]. Along the WER, both the eigenenergies and eigenvectors coalesce. Due to the ring-like structure of the topological defect, the topology of the parameter-space manifold depends upon its position, as well as upon its size, which is fundamentally distinct from that of a Hermitian system.

### III. EXPERIMENT AND RESULTS

We engineer the WER and demonstrate its topological feature using a circuit QED device with a bus resonator ( $R_b$ ) and 5 frequency-tunable qubits, one of which ( $Q$ ), together with its readout resonator ( $R$ ), is used to realize the spin-boson model.  $Q$  has an energy relaxation time  $T_1 \approx 14.3 \mu\text{s}$  and a pure Gaussian dephasing time  $T_2^* \approx 5.3 \mu\text{s}$  at its idle frequency  $\omega_I/2\pi = 6.0 \text{ GHz}$ , where it is transformed from the initial ground state  $|g\rangle$  to the excited state  $|e\rangle$  with a  $\pi$  pulse. During application of the pulse,  $Q$  is highly detuned and thus effectively decoupled from both  $R_b$  and  $R$  with frequencies  $\omega_b/2\pi = 5.584 \text{ GHz}$  and  $\omega/2\pi = 6.656 \text{ GHz}$ , respectively. The pulse sequence is sketched in the Supplemental Material. After this transformation,  $Q$  is coupled to  $R$  through application of an ac flux, modulating the qubit frequency as  $\omega_q = \omega_0 + \varepsilon \cos(\nu t)$  [25], where  $\omega_0$  is the mean frequency and  $\varepsilon$  ( $\nu$ ) is the modulation amplitude (frequency), respectively. The modulation frequency  $\nu \approx 2\pi \times (678.4 \sim 643.0) \text{ MHz}$  is close to  $\omega - \omega_0$ , so that  $Q$  is quasi-resonantly coupled to  $R$  at the first upper sideband of the modulation. The couplings at the carrier and other sidebands can be discarded due to large detunings. The system evolution is approximately governed by the Hamiltonian of Eq. (1) with the effective coupling  $\lambda = \lambda_r J_1(\mu)$  and the detuning  $\Delta = \nu + \omega_0 - \omega$ , where  $\mu = \varepsilon/\nu$ ,  $J_1(\mu)$  is the first-order Bessel function of the first kind, and  $\lambda_r = 2\pi \times 41 \text{ MHz}$  denotes the on-resonance coupling strength between the qubit and the readout resonator. The Hamiltonian parameters  $\Delta$  and  $\lambda$  are tunable by the parametric modulation pulse, and the non-Hermiticity is manifested by the photonic dissipation with a rate of  $\kappa = 5 \text{ MHz}$ . The decaying rates of  $Q$  and  $R_b$ ,  $0.07 \text{ MHz}$  and  $0.083 \text{ MHz}$ , are much smaller than  $\kappa$ , and thus can be discarded.

The topological features of the engineered WER are manifested by the quantized Berry phase of a loop encircling the WER, as well as by the Chern number of a manifold enclosing it. The Berry phase is defined as [12]

$$\beta_n = i \oint_{\mathcal{L}} \langle u_n^l(\mathbf{B}) | \frac{\partial}{\partial \mathbf{B}} | u_n^r(\mathbf{B}) \rangle \cdot d\mathbf{B}, \quad (6)$$

where the path  $\mathcal{L}$  travels across the ring twice along the loop in parameter space [Fig. 2(a)], so that the eigenvector returns to the original one after the entire trajectory. When the loop encircles the WER, the acquired Berry phase is  $\pm\pi$ , which becomes zero for a loop without encircling it. Due to the chiral nature associated with the

non-Hermiticity, the system does not adiabatically follow a specific eigenvector by slowly changing the control parameter. The breakdown of the adiabaticity prevents measurement of the Berry phase by adiabatic evolution. However, the Berry phase associated with each eigenvector is encoded in the parameter space, and has no direct relation to the evolution time. This enables us to infer the Berry phase by measuring the dependence of the eigenvector on the control parameter [25], without resorting to the adiabatic process.

The eigenvectors for a preset control parameter can be extracted from the joint  $Q$ - $R$  output states for different interaction times. When the modulation is switched off,  $Q$  is effectively decoupled from  $R$  due to large detuning. Then  $Q$ 's state is mapped to an ancilla qubit  $Q_a$  with the assistance of  $R_b$ , following which  $R$ 's state is transferred to  $Q$  through the modulation-induced sideband interaction. The resulting joint  $Q_a$ - $Q$  state projected to the single-excitation subspace, which can be measured by the quantum state tomography and postselection technique [25], corresponds to the  $Q$ - $R$  output state just before the state transfer procedure. The eigenvectors are inferred from the tracked time-evolving  $Q$ - $R$  output states, as detailed in the Supplemental Material. We choose circular loops centered at  $(B_z = 0, B_x = \kappa/2)$  on the  $B_x$ - $B_z$  plane. With this choice, whether or not the WER is encircled depends on the radius of the traversed loop ( $B_r$ ), as shown in Fig. 2(a). We can fit right eigenvectors  $|u_n^r(\mathbf{B})\rangle$  as functions of the control parameter  $\mathbf{B}$  with the results extracted for different settings of  $\mathbf{B}$ , and calculate the left vectors  $|u_n^l(\mathbf{B})\rangle$  using the biorthonormal condition. Fig. 2(b) shows the Berry phase ( $\beta_1$  and  $\beta_2$ ) for the two pairs of eigenvectors versus  $B_r$ . These Berry phases, measured at  $B_r = 0.427\kappa$ , are about  $-0.9844\pi$  and  $-0.9844\pi$ , respectively. With the shrinking of the loop, each of these Berry phases makes an abrupt change around  $B_r = 0.226\kappa$ , quickly dropping to 0 when crossing this critical point, thereby manifesting a topological transition.

Unlike previous implementations of WERs [18–22], in our system, the topological characteristic is encoded in the  $Q$ - $R$  quantum correlation. To demonstrate this non-classical characteristic, we calculate the concurrence from the inferred right eigenvectors for different control parameters during traversing the loop with the radius  $\kappa/2$ . The concurrence is a powerful measure of the quantum correlation between two two-level particles. The results are shown in Fig. 2(c), where  $\varphi$  is the angle between the control parameter  $\mathbf{B}$  and the  $x$ -axis. When  $\varphi$  is zero, the eigenvectors are maximally entangled states, with concurrence equal to 1. As  $\varphi$  increases, the concurrence of the eigenvectors decreases, thus indicating a reduction in quantum correlation. When  $\varphi$  reaches  $\pi$ , the system has no  $Q$ - $R$  interaction, and the concurrence is zero. As  $\varphi$  continues to increase, the concurrence begins to rise again, and returns to 1 when  $\varphi$  reaches  $2\pi$  where the system returns to its original parameter configuration. These results clearly demonstrate the geometric features

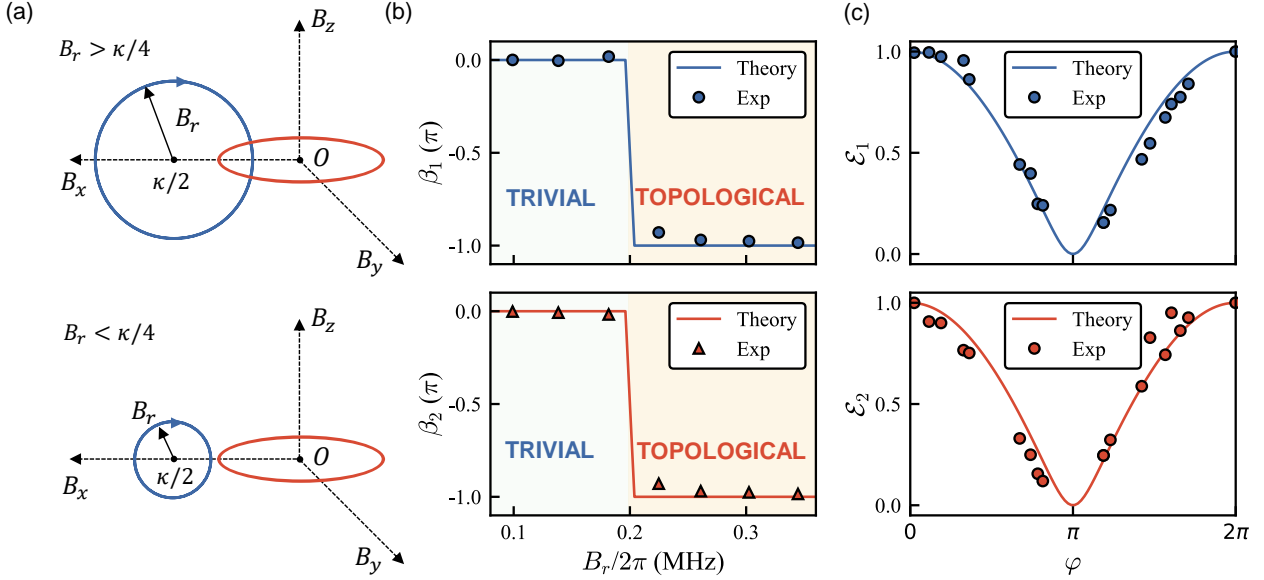


FIG. 2. Topological transition characterized with the Berry phase. (a) Loops associated with topologically distinct phases. The loops are circularly-shaped, and centered at  $(B_x = \kappa/2, B_z = 0)$  on the  $B_x$ - $B_z$  plane. The WER is encircled when the radius of the traversed loop ( $B_r$ ) is in the range  $(\kappa/4, 3\kappa/4)$ . (b) Measured Berry phase versus  $B_r$ . The dots and triangles denote the results associated with the two pairs of eigenvectors  $\{|u_n^r(\mathbf{B})\rangle, |u_n^l(\mathbf{B})\rangle\}$  with  $n = 1, 2$ . (c) Qubit-resonator concurrences versus the control parameter  $\mathbf{B}$ . The concurrences are obtained from the corresponding eigenstates. As the loop has a radius  $\kappa/2$ , the control parameter is determined by its angle ( $\varphi$ ) with respect to the  $x$ -axis.

are encoded in the entangled states of  $Q$  and  $R$ , illustrating the quantum-mechanical character of the measured Berry phase.

It is convenient to calculate the Chern number on a spherical manifold, which is centered at the origin of the parameter space. For a sphere with a specific radius  $B_r$ , the control parameters are the polar and azimuth angles  $(\theta, \phi)$ . The  $\phi$  and  $\theta$  components of the Berry connection are defined as

$$\begin{aligned} A_\phi^n &= i \langle u_n^r(\theta, \phi) | \partial_\phi | u_n^r(\theta, \phi) \rangle, \\ A_\theta^n &= i \langle u_n^r(\theta, \phi) | \partial_\theta | u_n^r(\theta, \phi) \rangle. \end{aligned} \quad (7)$$

The Chern number is given by

$$C_n = \frac{1}{2\pi} \int_0^{2\pi} d\phi \int_0^\pi d\theta F_{\theta\phi}^n, \quad (8)$$

where  $F_{\theta\phi}^n = \partial_\theta A_\phi^n - \partial_\phi A_\theta^n$  denotes the Berry curvature. When  $B_r > \kappa/4$ , the WER is enclosed in the manifold [Fig. 3(a)], so that the quantized Berry flux emanated from the WER pierces through the manifold, and the Chern number is  $\pm 1$ . For  $B_r < \kappa/4$ , the sphere is located inside the ring [Fig. 3(b)], the Berry flux entering the manifold and that going out of it cancel out each other, resulting in a zero Chern number. This unique feature does not exist for a point-like topological charge, and has not been experimentally observed so far.

Due to the spherical symmetry, the Berry connection  $A_\theta^n$  is independent of  $\phi$ , so that  $F_{\theta\phi}^n = \partial_\theta A_\phi^n$ . Taking

advantage of this symmetry, the Chern number can be obtained from the results measured along  $0^\circ$ -meridian [27, 28],

$$\begin{aligned} C_n &= \int_0^\pi d\theta \partial_\theta A_\phi^n \\ &= P_{e,0}^n(\pi) - P_{e,0}^n(0), \end{aligned} \quad (9)$$

where  $P_{e,0}^n(\theta)$  is the population of  $|e, 0\rangle$  in the eigenvector  $|u_n^r(\theta, 0)\rangle$ . With data of  $P_{e,0}^n$  measured for different values of  $\theta$ , we can fit the function  $P_{e,0}^n(\theta)$ , which are shown in Fig. 3(c) and (d). In our experiment, it is difficult to extract the eigenvectors when  $\lambda$  is small (see Supplemental Material for details). Here we calculate the Chern number using the  $P_{e,0}^n(\theta)$  with  $\theta$  lying as close to  $\pi$  and  $0$  as possible. Fig. 3(e) displays thus-obtained Chern numbers  $C_1$  and  $C_2$  versus the radius of the manifold. As expected, the Chern numbers, measured on a manifold with a radius larger than that of the WER  $\kappa/4$ , are equal to  $\pm 1$ . When  $B_r$  is reduced to the critical value of  $\kappa/4$ , a topological transition occurs, characterized by an abrupt drop of the Chern number to  $0$ . These results can be interpreted as follows. Under the condition that the WER is enclosed in the manifold, the eigenvector  $|u_n^r(\theta, 0)\rangle$  makes a  $\pi$  rotation, flipping from  $|g, 1\rangle$  ( $|e, 0\rangle$ ) to  $|e, 0\rangle$  ( $|g, 1\rangle$ ) following the variation of  $\theta$  from  $0$  to  $\pi$ , as illustrated in Fig. 3(c), where  $B_r/2\pi = 0.33$  MHz. In distinct contrast, for  $B_r < \kappa/4$ ,  $|u_n^r(\theta, 0)\rangle$  tilts away from vertical with an angle smaller than  $\pi/2$  and then returns [Fig. 3(d),  $B_r/2\pi = 0.18$  MHz]. The measured  $P_{e,0}^n$

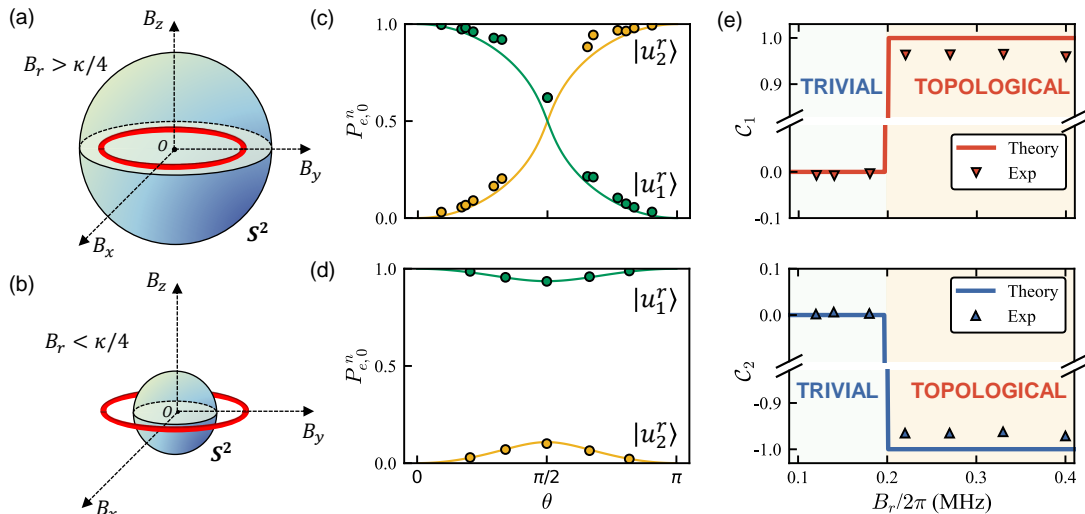


FIG. 3. Topological transition characterized with Chern number. (a), (b) Manifolds associated with topologically distinct phases. The spherical manifolds are centered at the origin of the 3D parameter space. When the WER is enclosed in the manifold (a), the quantized Berry flux emanated from the WER pierces through the manifold. When the sphere is located inside the ring (b), the amount of the Berry flux entering the manifold equals the amount going out of it. (c), (d) Measured populations of  $|e, 0\rangle$  in  $|u_n^r(\theta, \phi)\rangle$  ( $n = 1, 2$ ) versus  $\theta$  for  $B_r/2\pi = 0.33$  MHz (c) and 0.14 MHz (d). Here  $(B_r, \theta, \phi)$  denote the spherical coordinates for the control parameter. All data are measured for  $\phi = 0$ . The lines denote the functions fitted with the measured data. (e) Measured Chern number versus the radius of the manifold. The dots and triangles denote the results associated with the two right eigenvectors  $|u_1^r(\mathbf{B})\rangle$  and  $|u_2^r(\mathbf{B})\rangle$ , respectively.

versus  $\theta$  for different values of  $B_r$  are detailed in Supplemental Material. We note this topological behavior represents a unique characteristic that distinguishes the NH system from Hermitian ones, where a topological transition occurs only when the manifold is displaced so as not to enclose the origin of parameter—the diabolic point [26–34], but cannot be realized by shrinking the manifold centered at the diabolic point. This difference originates from the dissipation, which extends the point-like topological defect to a ring-like structure, significantly modifying the topological features of the parameter space.

#### IV. CONCLUSIONS

In conclusion, we have constructed a WER in a system composed of a qubit coupled to a resonator supporting a decaying photonic field, and characterized its topological features by the quantized Berry phase and Chern number, which are inferred from the measured eigenvectors of the governing NH Hamiltonian. We have observed

a topological phase transition featuring a change of the Chern numbers from  $\pm 1$  to 0, by continually reducing the size of the spherical manifold centered at the origin of the parameter space. Our results confirm that the non-Hermiticity changes a point-like degeneracy into a 2D ring of EPs, giving rise to exceptional topological phenomena that are absent in Hermitian systems. Our method can be generalized to realize the EP ring associated with a non-Abelian monopole and to explore NH topological transitions based on a higher-order Chern number.

#### ACKNOWLEDGMENTS

This work was supported by the National Natural Science Foundation of China (Grants No. 12274080, No. 12474356, No. 12475015, No. U21A20436) and Innovation Program for Quantum Science and Technology (Grants No. 2021ZD0300200, No. 2021ZD0301705).

- 
- [1] H. Weyl, GRAVITATION AND THE ELECTRON, *Proc. Natl. Acad. Sci.* **15**, 323 (1929).  
 [2] T. Kajita, Nobel Lecture: Discovery of atmospheric neutrino oscillations, *Rev. Mod. Phys.* **88**, 030501 (2016).  
 [3] M. Z. Hasan, S.-Y. Xu, I. Belopolski, and S.-M. Huang, Discovery of Weyl Fermion Semimetals and Topological

- Fermi Arc States, *Annu. Rev. Condens. Matter Phys.* **8**, 289 (2017).  
 [4] N. P. Armitage, E. J. Mele, and A. Vishwanath, Weyl and dirac semimetals in three-dimensional solids, *Rev. Mod. Phys.* **90**, 015001 (2018).

- [5] X. Wan, A. M. Turner, A. Vishwanath, and S. Y. Savrasov, Topological semimetal and fermi-arc surface states in the electronic structure of pyrochlore iridates, *Phys. Rev. B* **83**, 205101 (2011).
- [6] B. Q. Lv, H. M. Weng, B. B. Fu, X. P. Wang, H. Miao, J. Ma, P. Richard, X. C. Huang, L. X. Zhao, G. F. Chen, Z. Fang, X. Dai, T. Qian, and H. Ding, Experimental discovery of weyl semimetal taas, *Phys. Rev. X* **5**, 031013 (2015).
- [7] P. A. M. Dirac, Quantised singularities in the electromagnetic field, *Proc. R. Soc. Lond. A* **133**, 60 (1931).
- [8] M. V. Berry, Quantal phase factors accompanying adiabatic changes, *Proc. R. Soc. Lond. A* **392**, 45 (1984).
- [9] T. T. Wu and C. N. Yang, Concept of nonintegrable phase factors and global formulation of gauge fields, *Phys. Rev. D* **12**, 3845 (1975).
- [10] A. Szameit, M. C. Rechtsman, O. Bahat-Treidel, and M. Segev,  $\mathcal{PT}$ -symmetry in honeycomb photonic lattices, *Phys. Rev. A* **84**, 021806(R) (2011).
- [11] A. Cerjan, A. Raman, and S. Fan, Exceptional contours and band structure design in parity-time symmetric photonic crystals, *Phys. Rev. Lett.* **116**, 203902 (2016).
- [12] Y. Xu, S.-T. Wang, and L.-M. Duan, Weyl exceptional rings in a three-dimensional dissipative cold atomic gas, *Phys. Rev. Lett.* **118**, 045701 (2017).
- [13] T. Yoshida, R. Peters, N. Kawakami, and Y. Hatsugai, Symmetry-protected exceptional rings in two-dimensional correlated systems with chiral symmetry, *Phys. Rev. B* **99**, 121101(R) (2019).
- [14] T. Liu, J. J. He, Z. Yang, and F. Nori, Higher-order weyl-exceptional-ring semimetals, *Phys. Rev. Lett.* **127**, 196801 (2021).
- [15] S. A. A. Ghorashi, T. Li, and M. Sato, Non-hermitian higher-order weyl semimetals, *Phys. Rev. B* **104**, L161117 (2021).
- [16] M.-A. Miri and A. Alù, Exceptional points in optics and photonics, *Science* **363**, 7709 (2019).
- [17] Ş. K. Özdemir, S. Rotter, F. Nori, and L. Yang, Parity-time symmetry and exceptional points in photonics, *Nat. Mater.* **18**, 783 (2019).
- [18] E. J. Bergholtz, J. C. Budich, and F. K. Kunst, Exceptional topology of non-Hermitian systems, *Rev. Mod. Phys.* **93**, 015005 (2021).
- [19] K. Ding, C. Fang, and G. Ma, Non-hermitian topology and exceptional-point geometries, *Nat. Rev. Phys.* **4**, 745 (2022).
- [20] B. Zhen, C. W. Hsu, Y. Igarashi, L. Lu, I. Kaminer, A. Pick, S.-L. Chua, J. D. Joannopoulos, and M. Soljačić, Spawning rings of exceptional points out of Dirac cones, *Nature* **525**, 354 (2015).
- [21] A. Cerjan, S. Huang, M. Wang, K. P. Chen, Y. Chong, and M. C. Rechtsman, Experimental realization of a Weyl exceptional ring, *Nat. Photonics* **13**, 623 (2019).
- [22] J. J. Liu, Z. W. Li, Z. G. Chen, W. Tang, A. Chen, B. Liang, G. Ma, and J. C. Cheng, Experimental realization of weyl exceptional rings in a synthetic three-dimensional non-hermitian phononic crystal, *Phys. Rev. Lett.* **129**, 084301 (2022).
- [23] W. Tang, X. Jiang, K. Ding, Y.-X. Xiao, Z.-Q. Zhang, C. T. Chan, and G. Ma, Exceptional nexus with a hybrid topological invariant, *Science* **370**, 1077 (2020).
- [24] W. Tang, K. Ding, and G. Ma, Realization and topological properties of third-order exceptional lines embedded in exceptional surfaces, *Nat. Commun.* **14**, 6660 (2023).
- [25] P.-R. Han, F. Wu, X.-J. Huang, H.-Z. Wu, C.-L. Zou, W. Yi, M. Zhang, H. Li, K. Xu, D. Zheng, H. Fan, J. Wen, Z.-B. Yang, and S.-B. Zheng, Exceptional entanglement phenomena: Non-hermiticity meeting non-classicality, *Phys. Rev. Lett.* **131**, 260201 (2023).
- [26] P.-R. Han, W. Ning, X.-J. Huang, R.-H. Zheng, S.-B. Yang, F. Wu, Z.-B. Yang, Q.-P. Su, C.-P. Yang, and S.-B. Zheng, Measuring topological invariants for higher-order exceptional points in quantum multipartite systems, arXiv:2402.16169 (2024).
- [27] M. D. Schroer, M. H. Kolodrubetz, W. F. Kindel, M. Sandberg, J. Gao, M. R. Vissers, D. P. Pappas, A. Polkovnikov, and K. W. Lehnert, Measuring a topological transition in an artificial spin-1/2 system, *Phys. Rev. Lett.* **113**, 050402 (2014).
- [28] G. Jotzu, M. Messer, R. Desbuquois, M. Lebrat, T. Uehlinger, D. Greif, and T. Esslinger, Experimental realization of the topological Haldane model with ultracold fermions, *Nature* **515**, 237 (2014).
- [29] W. Tang, K. Ding, and G. Ma, Direct measurement of topological properties of an exceptional parabola, *Phys. Rev. Lett.* **127**, 034301 (2021).
- [30] X. Tan, D.-W. Zhang, Z. Yang, J. Chu, Y.-Q. Zhu, D. Li, X. Yang, S. Song, Z. Han, Z. Li, Y. Dong, H.-F. Yu, H. Yan, S.-L. Zhu, and Y. Yu, Experimental measurement of the quantum metric tensor and related topological phase transition with a superconducting qubit, *Phys. Rev. Lett.* **122**, 210401 (2019).
- [31] S. Sugawa, F. Salces-Carcoba, A. R. Perry, Y. Yue, and I. B. Spielman, Second Chern number of a quantum-simulated non-Abelian Yang monopole, *Science* **360**, 1429 (2018).
- [32] X. Tan, D.-W. Zhang, W. Zheng, X. Yang, S. Song, Z. Han, Y. Dong, Z. Wang, D. Lan, H. Yan, S.-L. Zhu, and Y. Yu, Experimental observation of tensor monopoles with a superconducting qudit, *Phys. Rev. Lett.* **126**, 017702 (2021).
- [33] M. Chen, null, C. Li, G. Palumbo, Y.-Q. Zhu, N. Goldman, and P. Cappellaro, A synthetic monopole source of kalb-ramond field in diamond, *Science* **375**, 1017 (2022).
- [34] M. Yu, P. Yang, M. Gong, Q. Cao, Q. Lu, H. Liu, S. Zhang, M. B. Plenio, F. Jelezko, T. Ozawa, N. Goldman, and J. Cai, Experimental measurement of the quantum geometric tensor using coupled qubits in diamond, *Nat. Sci. Rev.* **7**, 254 (2019).

# Supplementary Material for “Observation of topological transitions associated with a Weyl exceptional ring”

Hao-Long Zhang,<sup>1,\*</sup> Pei-Rong Han,<sup>1,\*</sup> Xue-Jia Yu,<sup>1,\*</sup> Shou-Bang Yang,<sup>1</sup> Jia-Hao Lü,<sup>1</sup> Wen Ning,<sup>1,†</sup> Fan Wu,<sup>1</sup> Qi-Ping Su,<sup>2</sup> Chui-Ping Yang,<sup>2</sup> Zhen-Biao Yang,<sup>1,3,‡</sup> and Shi-Biao Zheng<sup>1,3,§</sup>

<sup>1</sup>*Fujian Key Laboratory of Quantum Information and Quantum Optics,  
College of Physics and Information Engineering, Fuzhou University, Fuzhou 350108, China*

<sup>2</sup>*School of Physics, Hangzhou Normal University, Hangzhou 311121, China*

<sup>3</sup>*Hefei National Laboratory, Hefei 230088, China*

## CONTENTS

S1. Engineering of the dissipative Jaynes-Cummings model	1
S2. System parameters and pulse sequence	2
S3. Realization of longitudinal modulation and detuning of qubits frequency	3
S4. Correction for state mapping	4
S5. Measurement of eigenvectors	5
S6. Extraction of the Berry phase	7
S7. Extraction of the Chern number	8
References	8

## S1. ENGINEERING OF THE DISSIPATIVE JAYNES-CUMMINGS MODEL

The dissipative Jaynes-Cummings (JC) model is engineered in a circuit quantum electrodynamics architecture, where a bus resonator ( $R_b$ ) is connected to 5 Xmon qubits, each of which is individually connected to a readout resonator. The schematic diagram of the device is shown in Fig. S1(a). One of these qubits ( $Q$ ) and its readout resonator ( $R$ ) are used to construct the JC model. Another qubit ( $Q_a$ ) is used as an ancilla for reading out  $R$ 's state. The photonic swapping between  $Q$  and  $R$  is mediated by applying an ac flux to  $Q$ , modulating its frequency as

$$\omega_q = \omega_0 + \varepsilon \cos(\nu t), \quad (\text{S1})$$

where  $\omega_0$  is the mean frequency and  $\varepsilon$  ( $\nu$ ) is the modulation amplitude (frequency). The Hamiltonian of the  $Q$ - $R$  system is given by (setting  $\hbar = 1$ )

$$H = \omega_r a^\dagger a + \omega_q |e\rangle \langle e| + (\lambda_r a^\dagger |g\rangle \langle e| + H.c.), \quad (\text{S2})$$

where  $a^\dagger$  and  $a$  denote the creation and annihilation operators for the photonic field stored in  $R$ ,  $|e\rangle$  and  $|g\rangle$  are the excited and ground states of  $Q$ , and  $\lambda_r$  is the on-resonance  $Q$ - $R$  coupling strength. We here have assumed that  $Q$  is highly detuned from  $R_b$  and the other qubits, so that the  $Q$ - $R$  dynamics are unaffected by them.

Under the condition  $|\Delta| \ll \lambda_r$  where  $\Delta = \omega_0 + \nu - \omega_r$ ,  $Q$  swaps photons with  $R$  at the first upper sideband with respect to the modulation. To derive the effective Hamiltonian, we perform the transformation  $e^{i \int_0^t H_0 dt}$ , where  $H_0 = (\omega_q - \Delta) |e\rangle \langle e| + \omega_r a^\dagger a$ . Then the Hamiltonian is

$$H_S = \Delta |e\rangle \langle e| + \left[ e^{-i\mu \sin(\nu t)} e^{i\delta t} \lambda_r a^\dagger |g\rangle \langle e| + H.c. \right], \quad (\text{S3})$$

\* These authors contribute equally to this work.

† ningw@fzu.edu.cn

‡ zbyang@fzu.edu.cn

§ t96034@fzu.edu.cn

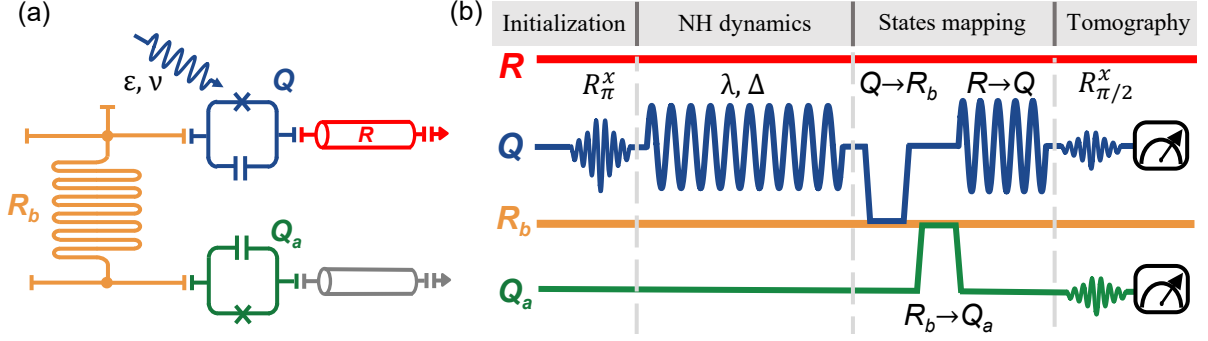


FIG. S1. (a) Implementation of the NH Hamiltonian. In the experimental system, a superconducting qubit  $Q$  is highly detuned from the decaying resonator  $R$ , which has a fixed frequency  $\omega_r/2\pi = 6.656$  GHz. The  $Q$ - $R$  interaction is enabled by an ac flux, which modulates  $Q$ 's energy gap around the mean value  $\omega_0$  with a frequency  $\nu$ . This modulation enables a photonic swapping coupling at one sideband, with the coupling strength controlled by the modulating amplitude  $\varepsilon$ . (b) Pulse sequence. The NH dynamics are initiated with the state  $|e, 0\rangle$  prepared by performing a  $\pi$  pulse on  $|g, 0\rangle$ . After the NH dynamics process, we perform the state mappings  $Q \rightarrow R_b$ ,  $R_b \rightarrow Q_a$ , and  $R \rightarrow Q$ , each realized by an on-resonance swapping gate. Here,  $Q_a$  is an ancilla qubit, and  $R_b$  represents the bus resonator coupled to both qubits. Through this method, the  $Q$ - $R$  output state produced by the NH dynamics is encoded in the joint  $Q_a$ - $Q$  state, which can be measured by quantum state tomography.

where  $\mu = \varepsilon/\nu$  and  $\delta = \omega_r - (\omega_0 - \Delta)$ . With the application of the Jacobi-Anger expansion  $e^{-i\mu \sin(\nu t)} = \sum_{n=-\infty}^{\infty} J_n(\mu)e^{-in\nu t}$ , the Hamiltonian (S3) can be expressed as

$$H_S = \Delta |e\rangle \langle e| + \sum_{n=-\infty}^{\infty} [J_n(\mu)e^{-in\nu t} e^{i\delta t} \lambda_r a^\dagger |g\rangle \langle e| + H.c.], \quad (\text{S4})$$

where  $J_n(\mu)$  is the  $n$ th Bessel function of the first kind. With the choice  $\delta = \nu$  and for  $\lambda_r \ll \nu$ , the terms (with  $n \neq 1$ ) oscillating fast can be discarded. Then the Hamiltonian (S4) reduces to

$$H_S = \Delta |e\rangle \langle e| + (\lambda a^\dagger |g\rangle \langle e| + H.c.), \quad (\text{S5})$$

where  $\lambda = \lambda_r J_1(\mu)$ .

Suppose that the energy dissipation rate of  $Q$  is much smaller than the photonic decaying rate of  $R$ , and thus can be neglected. Under the competition between the coherent dynamics and the photonic dissipation of  $R$ , the system evolution is described by the master equation

$$\frac{d\rho}{dt} = -i[H_{NH}, \rho] + \kappa \rho a^\dagger, \quad (\text{S6})$$

where

$$H_{NH} = H_S - \frac{i\kappa}{2} a^\dagger a. \quad (\text{S7})$$

For the initial state  $|e, 0\rangle$ , the system output state is a mixture of the  $Q$ - $R$  entangled state in the subspace  $\{|e, 0\rangle, |g, 1\rangle\}$  and the state  $|g, 0\rangle$ , which is produced by the photon-loss-induced quantum jump. The quantum state evolution trajectory without any quantum jump is governed by the NH Hamiltonian  $H_{NH}$ .

## S2. SYSTEM PARAMETERS AND PULSE SEQUENCE

$R$  has a fixed frequency  $\omega_r/2\pi = 6.656$  GHz and a photonic decaying rate  $\kappa = 5$  MHz, which is much larger than  $Q$ 's energy relaxation rate  $\gamma = 0.07$  MHz. The frequency and photonic decaying rate of  $R_b$  are  $\omega_b/2\pi = 5.584$  GHz and  $\kappa = 0.083$  MHz, respectively. Before the experiment,  $Q$  is initialized to the ground state at its idle frequency  $\omega_I/2\pi = 6.00$  GHz, where  $Q$  is effectively decoupled from  $R$  ( $R_b$ ) as the detuning  $2\pi \times 656$  MHz ( $2\pi \times 416$  MHz) is much larger than the on-resonance  $Q$ - $R$  ( $Q$ - $R_b$ ) coupling strength, which is  $2\pi \times 41$  MHz ( $2\pi \times 20.9$  MHz).

The experiment involves three parts: preparation of the initial state, controlled  $Q$ - $R$  NH dynamics, and output state tomography, as sketched in Fig. S1(b). The initial state  $|e, 0\rangle$  is prepared by applying a  $\pi$  pulse to  $Q$ . This is

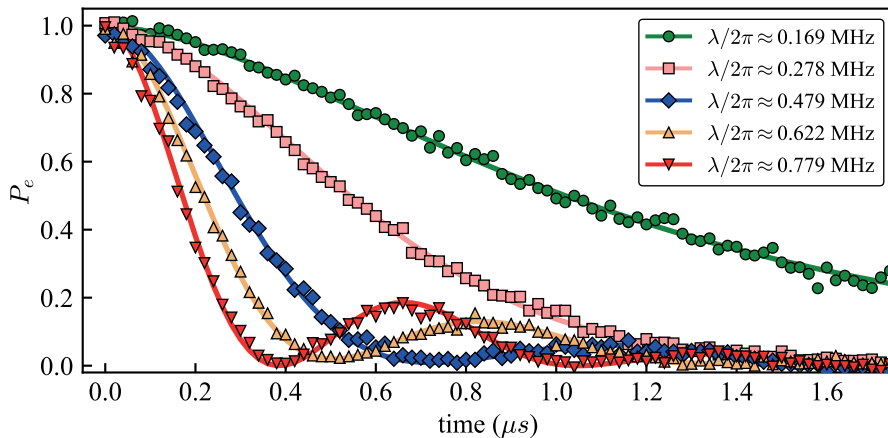


FIG. S2. Temporal evolution of the population  $P_e$  under different longitudinal modulations. The lines denote the fitting results and the dots represent the experimental results.

followed by the application of the parametric modulation to  $Q$ , mediating a sideband interaction between  $Q$  and  $R$  to realize the effective Hamiltonian  $H_S$  of Eq. (S5), with the parameters  $\Delta$  and  $\lambda$  controllable by the modulation frequency  $\nu$  and amplitude  $\varepsilon$ . During this sideband interaction, all the other qubits stay at their idle frequencies. The detuning between their idle frequencies and the frequency of  $Q$  range from  $2\pi \times 1.2$  GHz to  $2\pi \times 1.4$  GHz, much larger than their couplings with  $Q$  mediated by  $R_b$ , which are on the order of 1 MHz. These large detunings effectively decouple these qubits from  $Q$  during the  $Q$ - $R$  sideband interaction.

After a preset interaction time, the modulation pulse is switched off, following which a joint state tomography is performed. However,  $R$ 's quantum state cannot be directly read out. To overcome this problem, we transfer  $Q$ 's state to  $R_b$  by a swapping operation, realized by tuning  $Q$  and  $R_b$  on resonance for a time  $\pi/(2g)$ , where  $g$  is their coupling strength. Following this, the state of  $R_b$  is mapped to an ancilla qubit  $Q_a$ . Then  $R$ 's state is transferred to  $Q$  through the first sideband interaction. The resulting joint  $Q_a$ - $Q$  state, corresponding to  $Q$ - $R$  state before the state transfer procedure, can be measured by quantum state tomography.

### S3. REALIZATION OF LONGITUDINAL MODULATION AND DETUNING OF QUBITS FREQUENCY

In superconducting quantum platforms, the qubit transition frequency is modulated by an ac flux, generated by applying a pulse to the Z line. In our superconducting sample, the qubit transition frequency needs to be periodically modulated at a frequency  $\nu/2\pi > 0.65$  GHz, as specified in Eq. (S1). If the ac flux is modulated away from the sweet spot  $\omega_m$  [S1], the modulation frequency  $\nu$  of the qubit equals the frequency of the ac flux, which does not meet the experimental requirement given the limitations of our current hardware. To address this issue, we bias the flux to the sweet spot before applying longitudinal modulation. The modulation frequency of the qubit, achieved by modulating the flux at the sweet spot, is twice as high as that away from the sweet spot, enabling us to reach the desired modulation frequency. However, this method imposes an additional constraint,  $\omega_r - \omega_0 = \omega_m - \varepsilon$ , which restricts us in controlling the detuning  $\Delta$  between  $Q$  and  $R$  by adjusting the mean frequency of the qubit.

For specific values of  $\Delta$  and  $\lambda$ , we need to determine the corresponding values of modulation parameters to realize the effective Hamiltonian  $H_S$ . Initially, we need to determine the longitudinal modulation frequency  $\nu$  and amplitude  $\varepsilon$  that correspond to the effective coupling strength  $\lambda$ . Disregarding the detuning  $\Delta$  ( $\Delta = 0$ ), the coherent dynamics of the system comprising  $Q$  and  $R$  is governed by Eq. (S5). Due to the additional constraints mentioned above, the modulation frequency  $\nu$ , the amplitude  $\varepsilon$ , and the mean frequency  $\omega_0$  are deterministically related to the effective coupling strength  $\lambda$  in a one-to-one manner.

To determine this relationship, we first prepare  $Q$  in the excited state  $|e\rangle$ , and then apply a longitudinal modulation while keeping  $\varepsilon$  fixed. We observe oscillatory behavior in the population of the state  $|e\rangle$  of the qubit over time for various modulation frequencies  $\nu$ . By identifying the point where the exchange between  $Q$  and  $R$  is almost complete, such set of  $\nu$  and  $\varepsilon$  determines an effective coupling between  $Q$  and  $R$ . Subsequently, the effective coupling strength  $\lambda$  under this parameter configuration is obtained by fitting the population of the state  $|e\rangle$  using Eq. (S5) with  $\Delta = 0$ . This process is repeated with finite-tuning  $\nu$  and  $\varepsilon$  until all necessary values for  $\lambda$  are obtained. To validate these modulations, we present the vacuum Rabi oscillation signals for the test qubit  $Q$  induced by these sideband couplings

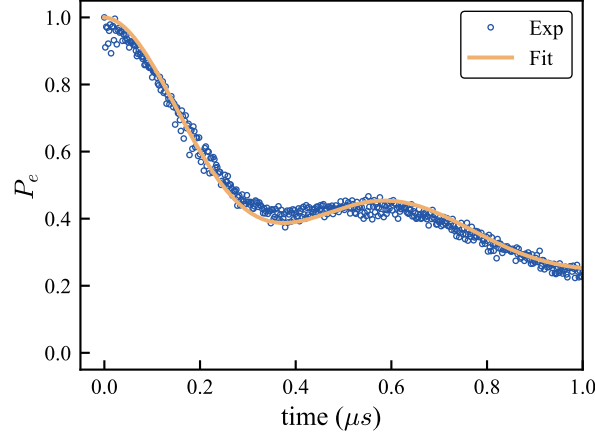


FIG. S3. The fitting results of calibration to parameters  $\Delta$  and  $\lambda$ . The orange lines denote the fitting results and the dots represent the experimental results.

for different modulating amplitudes in Fig. S2. Due to imperfections in the longitudinal modulation pulse, directly adjusting the mean frequency of the qubits by changing  $\varepsilon$  becomes challenging. Instead, we achieve detuning by fine-tuning the frequency  $\nu$  of the periodic modulation after observing first-order sideband resonances between  $Q$  and  $R$ . At the point, it has  $\nu = \omega_r - \omega_0$ ,  $\mu = \varepsilon/\nu$  and  $\lambda = \lambda_r J_1(\mu)$ . Then the Hamiltonian is

$$H = e^{-i\mu' \sin[(\nu+\Delta)t]} e^{i(\omega_r - \omega_0)t} \lambda_r a^\dagger |g\rangle \langle e| + H.c., \quad (\text{S8})$$

where  $\mu' = \varepsilon/(\nu + \Delta)$ . By use of the Jacobi-Anger expansion, the Hamiltonian becomes

$$H = \sum_{n=-\infty}^{\infty} J_n(\mu') e^{-in(\nu+\Delta)t} e^{i(\omega_r - \omega_0)t} \lambda_r a^\dagger |g\rangle \langle e| + H.c.. \quad (\text{S9})$$

The terms (with  $n \neq 1$ ) oscillating fast can be discarded, thus  $H$  reduces to

$$H_S = \Delta |e\rangle \langle e| + (\lambda' a^\dagger |g\rangle \langle e| + H.c.), \quad (\text{S10})$$

where  $\lambda' = \lambda_r J_1(\mu') \neq \lambda$ . The effective coupling  $\lambda$ , in this case, deviates slightly from our preset value due to the imperfections of the modulated pulses, e.g., when we adjust the modulation frequency of qubit  $\nu$ , the corresponding  $\varepsilon$  for the same pulse amplitude also experiences slight changes. Therefore, to obtain more accurate values for  $\Delta$  and  $\lambda$ , we perform a preliminary fitting of the experimental data.

#### S4. CORRECTION FOR STATE MAPPING

As the excitation number is conserved under the NH Hamiltonian  $H_{NH}$ , for the initial state  $|e, 0\rangle$ , we can postselect the output state without undergoing any quantum jump by discarding the measurement output, where both  $Q$  and  $Q_a$  are in their ground states. However, due to the strong dissipation of  $R$ , the  $Q_a$ - $Q$  state after the state mapping does not perfectly coincide with the  $Q$ - $R$  state just before the mapping.

Suppose that the  $Q$ - $R$  output state, associated with the no-jump trajectory governed by the NH Hamiltonian  $H_{NH}$ , is

$$|\psi_{NH}\rangle = \alpha |e, 0\rangle + \beta |g, 1\rangle. \quad (\text{S11})$$

After the state mapping, the  $Q_a$ - $Q$  output state is

$$|\psi'_{NH}\rangle = \alpha' |e_a, g\rangle + \beta' |g_a, e\rangle, \quad (\text{S12})$$

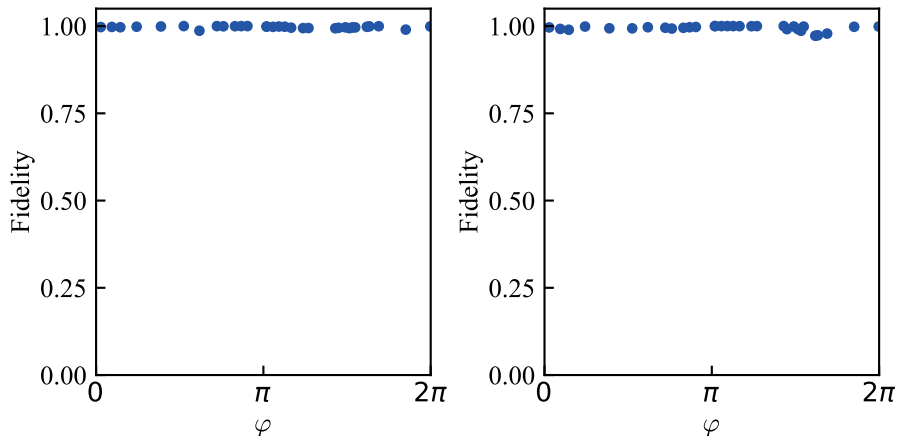


FIG. S4. Fidelities of fitted eigenvectors. (a)  $\mathcal{F}_0$  as a function of  $\varphi$ . (b)  $\mathcal{F}_1$  as a function of  $\varphi$ .

where

$$\alpha' = \frac{\alpha}{\sqrt{|\alpha|^2 + \beta e^{-\kappa(t_1+t_2/2)}}}, \quad (\text{S13})$$

$$\beta' = \frac{\beta e^{-\kappa(t_1/2+t_2/4)}}{\sqrt{|\alpha|^2 + \beta e^{-\kappa(t_1+t_2/2)}}}, \quad (\text{S14})$$

with  $t_1$  being the duration for the  $Q \rightarrow R_b \rightarrow Q_a$  state mapping, and  $t_2$  denoting the duration for the  $R \rightarrow Q$  mapping. Given that  $t_1 \ll t_2$ , we only consider  $t_2$  and set  $t_2 = 118$  ns in our experiment. We here neglect the dissipations of  $Q$ ,  $R_b$ , and  $Q_a$ . This implies that we can infer the coefficients  $\alpha$  and  $\beta$  from the measured values of  $\alpha'$  and  $\beta'$ .

### S5. MEASUREMENT OF EIGENVECTORS

As mentioned in Sec. S3, due to the experimental imperfections, the parameters  $\Delta$  and  $\lambda$  may have minor errors compared to the theoretical predictions obtained by the experimental parameters  $\nu$  and  $\varepsilon$ . To calibrate these errors, we prepare the initial state  $|e, 0\rangle$  and measure the evolution of the population of  $|e\rangle$  with the predicted parameters  $\lambda_i$  and  $\Delta_i$ . We then fit this population to obtain the calibrated parameters  $\lambda_c$  and  $\Delta_c$  based on the error function

$$F_{\text{err}}^1 = \sum_{i=1}^N [P_{e,i}^{\text{exp}}(t_i) - P_{e,i}^{\text{the}}(t_i)]^2 / N, \quad (\text{S15})$$

where  $P_{e,i}^{\text{exp}}(t_i)$  is the evolution of the population of  $|e\rangle$  at the moment  $t_i$  and  $P_{e,i}^{\text{the}}(t_i)$  is the corresponding theoretical result. Based on this error function, the next step is to seek the fitting parameters to minimize the value of the error function. This allows us to obtain the calibrated parameters  $\lambda_c$  and  $\Delta_c$ . The fitting results are shown in Fig. S3, demonstrating the validity of this method.

After the calibration of the parameters  $\Delta$  and  $\lambda$ , we can extract the corresponding eigenvectors of this system. The final state  $|\psi_{NH}\rangle$  can be written as

$$|\psi_{NH}\rangle = \mathcal{N} (C_1 e^{-iE_1 t} |u_1^r\rangle - C_2 e^{-iE_2 t} |u_2^r\rangle), \quad (\text{S16})$$

where  $\mathcal{N}$  is the normalization coefficient, the coefficients  $C_n$  ( $n = 1, 2$ ) are given by

$$C_n = \frac{\sqrt{|\lambda|^2 + |E_n - \Delta|^2}}{E_n - \Delta}, \quad (\text{S17})$$

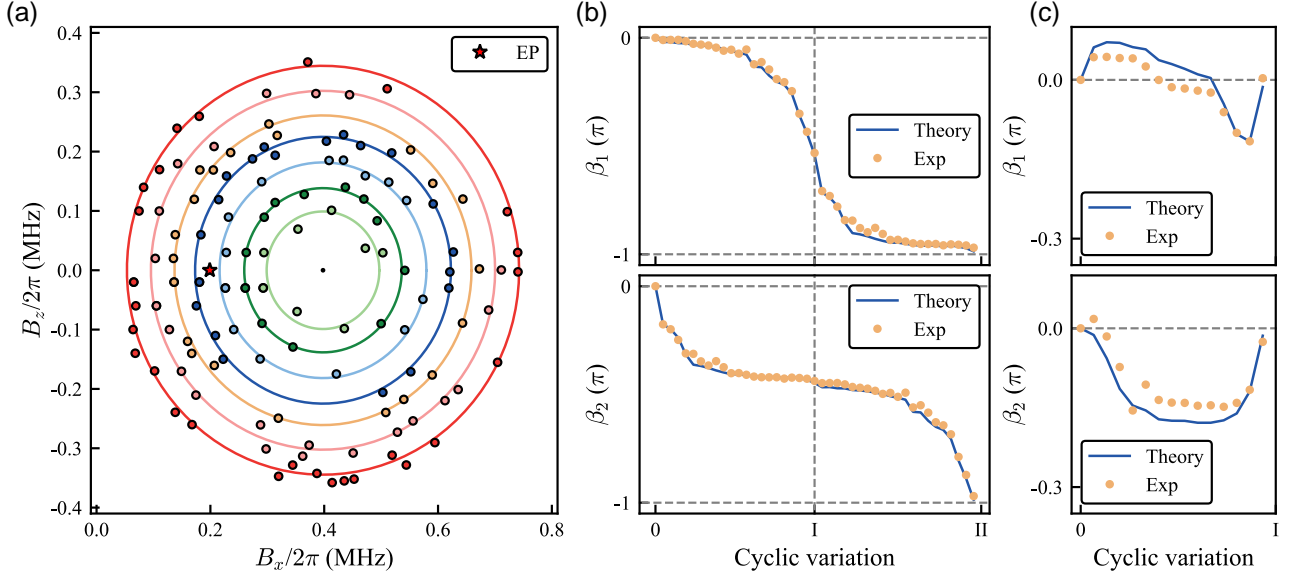


FIG. S5. (a) The summation path of the Berry phase on the  $B_x$ - $B_z$  plane ( $B_y = 0$ ) for  $B_r/2\pi = 0.10, 0.14, 0.18, 0.22, 0.26, 0.30, 0.34$  MHz. The red star marks the exceptional point. The lines denote the theoretical paths and the dots represent the experimental parameters. (b)(c) The corresponding Berry phase after two cycles ( $B_r/2\pi = 0.26$  MHz) and one cycle ( $B_r/2\pi = 0.18$  MHz), respectively. The dots represent the experimental data and the solid lines denote the theoretical results for the experimental parameters.

$E_{1,2} = \pm\sqrt{|\lambda|^2 + (2\Delta + i\kappa)^2/16}$  are the eigenenergies,  $t$  is the interaction time, and  $|u_n^r\rangle$  ( $n = 1, 2$ ) denote the right eigenvectors, which can be written as

$$|u_n^r\rangle = \frac{\lambda^* |e, 0\rangle + (E_n - \Delta) |g, 1\rangle}{\sqrt{|\lambda|^2 + |E_n - \Delta|^2}}. \quad (\text{S18})$$

The relation between the output state  $|\psi_{NH}\rangle$  and  $|u_n^r\rangle$  implies that  $|u_n^r\rangle$  can be extracted from  $|\psi_{NH}\rangle$ , measured for different interaction times. We obtain  $|u_n^r\rangle$  through the least-squares fitting to the output density matrices measured and post-projected to the single-excitation subspace [S2].

For a certain point in the parameter space of the NH system, the eigenenergies and the corresponding eigenvectors can be written as

$$E_n = a_n + ib_n, \quad |u_n^r\rangle = \sqrt{1 - c_n^2} |g, 1\rangle + c_n e^{id_n} |e, 0\rangle, \quad (\text{S19})$$

where  $a_n, b_n, c_n$  and  $d_n$  are the fitting parameters ( $n = 1, 2$ ). To minimize the fitting errors, we define an error function as guidance, which has the form of

$$F_{\text{err}}^2 = \text{Tr}[\rho |\psi_{NH}\rangle \langle \psi_{NH}|] - 1. \quad (\text{S20})$$

Based on this error function, the next step is to seek the fitting parameters that can minimize Eq. (S20) at each moment. In this way, a reliable least-squares fitting to the entire evolution of the density matrix  $\rho$  is found with all the parameters.

To demonstrate the validity of this method, we calculate the fidelities of the eigenvectors for the theoretical results along the circular loops, which are centered at  $(B_x = \kappa/2, B_z = 0)$  on the  $B_x - B_z$  plane, that is

$$\mathcal{F}_n(\varphi) = |\langle u_n^{r'}(\varphi) | u_n^r(\varphi) \rangle|^2, \quad (\text{S21})$$

where  $|u_n^{r'}\rangle$  are the theoretical eigenvectors. In our experiment, we set the radius of the circle  $B_r \approx 0.34\kappa$  and calculate the function with different angles  $\varphi$  between the control parameter  $\mathbf{B}$  and the x-axis. As shown in Fig. S4, the results demonstrate that the eigenstates, extracted from the measured two-qubit output density matrices by our density-matrix post-projecting method, well agree with the ideal ones, associated with the no-jump evolution trajectories. With thus-obtained right eigenvectors, the left eigenvectors can be obtained from the biorthonormal condition:

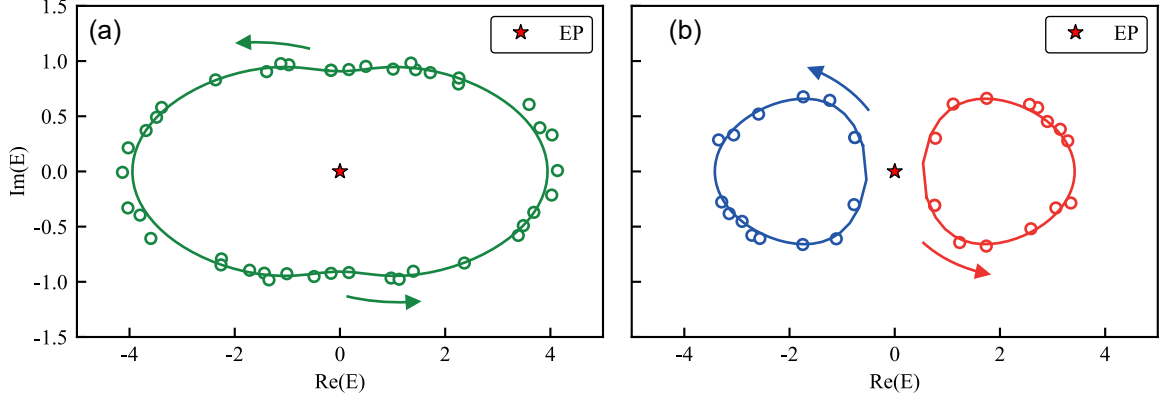


FIG. S6. (a) The spectrum along the summation path of the Berry phase across two cycles ( $B_r/2\pi = 0.26$  MHz). Due to the eigenvectors exchange, the spectrum's summation path  $E_1$  is the same as one of  $E_2$ , here we only show one of the spectrum. (b) The spectrum along the summation path of the Berry phase across one cycle for  $E_1$  (left circle) and  $E_2$  (right circle) ( $B_r/2\pi = 0.18$  MHz), respectively. The red star marks the exceptional point. The dots represent the experimental data and the solid lines denote the theoretical results for the experimental parameters.

$$\langle u_n^l | u_m^r \rangle = \delta_{m,n}. \quad (\text{S22})$$

### S6. EXTRACTION OF THE BERRY PHASE

Using the right and left eigenvectors, we can obtain the Berry phase along the path  $2\mathcal{L}$  across the ring twice on the Riemann surface [Fig. 2(a)],

$$\beta_n = i \oint_{2\mathcal{L}} \langle u_n^l(\mathbf{B}) | \frac{\partial}{\partial \mathbf{B}} | u_n^r(\mathbf{B}) \rangle \cdot d\mathbf{B}. \quad (\text{S23})$$

In our experiment, we choose circular loops centered at  $(B_x = \kappa/2, B_z = 0)$  on the  $B_x$ - $B_z$  plane and approximately calculate the Berry phase versus radius  $B_r$  through the discretized summation

$$\beta_n(B_r) = i \sum_{p=1}^{2\mathcal{P}} \langle u_{n,p}^l(B_r) | \frac{|u_{n,p+1}^r(B_r)\rangle - |u_{n,p}^r(B_r)\rangle}{\Delta\varphi} \Delta\varphi, \quad (\text{S24})$$

where  $\varphi$  is the angle between the control parameter  $\mathbf{B}$  and the x-axis, and  $\mathcal{P}$  is the number of steps for traversing each cycle. The loop with different radius  $B_r$  on the  $B_x$ - $B_z$  plane is shown in Fig. S5(a). Experimentally, the system is excited independently at each step  $p$  during stationary-state measurements. The eigenvectors, obtained from these measurements, inevitably carry random phase factors. To track the evolution of the Berry phase in the intermediate steps ( $p > 1$ ), we rotate the right eigenvector  $|u_{n,p+1}^r\rangle$  by a phase factor  $\phi_n^{p+1} = -\arg[\ln\langle u_{n,p+1}^l | \bar{u}_{n,p}^r \rangle]$  for each intermediate step  $p$ , thus removing the arbitrary phase [S3]

$$|\bar{u}_{n,p+1}^r\rangle = e^{i\phi_n^{p+1}} |u_{n,p+1}^r\rangle. \quad (\text{S25})$$

As a result,  $\langle \bar{u}_{n,p+1}^l | u_{n,p}^r \rangle$  is real and positive, satisfying the condition of parallel transport. For the initial step  $p = 1$ , we set  $|\bar{u}_{n,p=1}^r\rangle = |u_{n,p=1}^r\rangle$ , indicating the initial phase factor is carried along the path  $2\mathcal{L}$ . This method allows us to track the Berry phase's evolution, shown in Fig. S5(b) and (c). The spectrum along the path is shown in Fig. S6. When  $B_r > \kappa/4$ , the WER is encircled, and the eigenvectors exchange occurs near  $\varphi = \pi$ . After the completion of two cycles [Fig. S6(a)], the eigenvector is restored and obtains a phase difference, approaching  $-\pi$ , which is the Berry phase. However, when  $B_r < \kappa/4$ , the WER is not encircled and there is no eigenvectors exchange. So the eigenvector is fully restored in only one complete cycle [Fig. S6(b)]. And the corresponding Berry phase drops to 0.

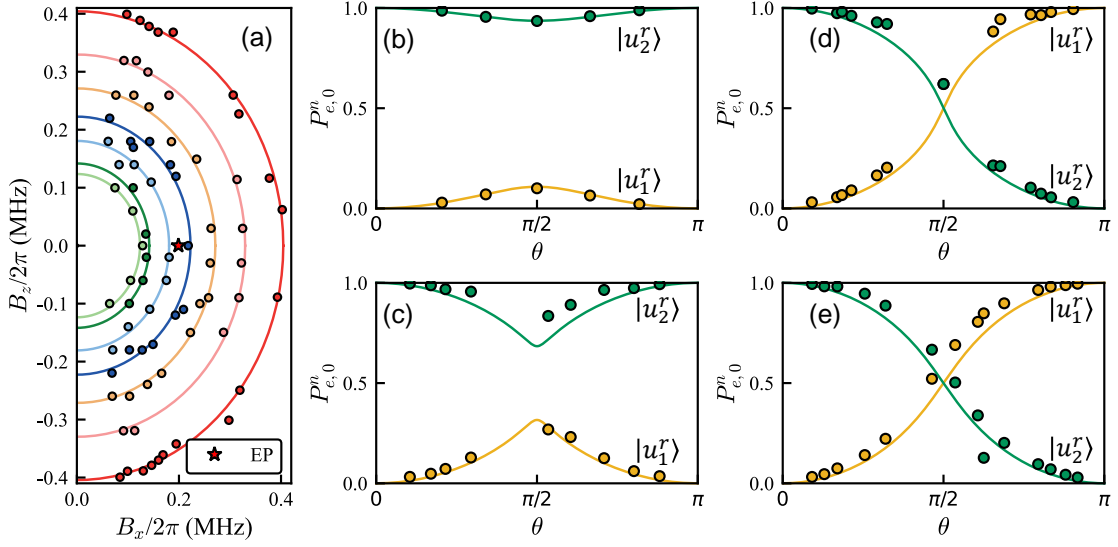


FIG. S7. (a) The summation path of the Chern number on the  $B_x$ - $B_z$  plane ( $B_y = 0$ ) for  $B_r/2\pi = 0.12, 0.14, 0.18, 0.22, 0.27, 0.32, 0.40$  MHz. The red star marks the exceptional point. The lines denote the theoretical path and the dots represent the experimental parameters. Measured populations of  $|e, 0\rangle$  in  $|u_n\rangle$  ( $n = 1, 2$ ) versus  $\theta$  for  $B_r/2\pi = 0.12$  MHz (b), 0.18 MHz (c), 0.22 MHz (d), 0.27 MHz (e).

### S7. EXTRACTION OF THE CHERN NUMBER

The Chern number is calculated on a spherical manifold, which is centered at the origin of the parameter space, i.e.,

$$C_n(B_r) = \frac{1}{2\pi} \int_0^{2\pi} d\phi \int_0^\pi d\theta F_{\theta\phi}^n(B_r, \theta, \phi), \quad (\text{S26})$$

where  $B_r$  is the radius of the sphere,  $\theta$  ( $\phi$ ) is the polar (azimuth) angle, and  $F_{\theta\phi}^n(B_r, \theta, \phi)$  is the Berry curvature. The Berry curvature can be calculated by the Berry connection

$$F_{\theta\phi}^n(B_r, \theta, \phi) = \partial_\theta A_\phi^n - \partial_\phi A_\theta^n, \quad (\text{S27})$$

where  $A_\phi^n = i\langle u_n(B_r, \theta, \phi) | \partial_\phi | u_n(B_r, \theta, \phi) \rangle$  and  $A_\theta^n = i\langle u_n(B_r, \theta, \phi) | \partial_\theta | u_n(B_r, \theta, \phi) \rangle$ . In our experiment, due to the spherical symmetry, the Berry connection is independent of  $\phi$ , so that  $F_{\theta\phi}^n(B_r, \theta) = \partial_\theta A_\phi^n(B_r, \theta)$ . The corresponding Chern number is

$$\begin{aligned} C_n(B_r) &= \frac{1}{2\pi} \int_0^{2\pi} d\phi \int_0^\pi d\theta F_{\theta\phi}^n(B_r, \theta, \phi) \\ &= \int_0^\pi d\theta \partial_\theta A_\phi^n(B_r, \theta) \\ &= P_{e,0}^n(B_r, \pi) - P_{e,0}^n(B_r, 0), \end{aligned} \quad (\text{S28})$$

where  $P_{e,0}^n(B_r, \theta)$  is the population of  $|e, 0\rangle$  in the eigenvector  $|u_n^r(B_r, \theta, 0)\rangle$ . The paths with different radius  $B_r$  we choose to fit the function  $P_{e,0}^n$  are shown in Fig. S7(a), and the fitting results  $P_{e,0}^n(\theta)$  for different radius  $B_r$  are shown in Fig. S7(b)-(e). Extracting the eigenvector using the method described in Sec. S5 is challenging when  $\lambda$  is small. Therefore, we calculate the Chern number using  $P_{e,0}^n(\theta)$ , where  $\theta$  is chosen to be as close to  $\pi$  and 0 as possible.

---

[S1] P. Krantz, M. Kjaergaard, F. Yan, T. P. Orlando, S. Gustavsson, and W. D. Oliver, A quantum engineer's guide to superconducting qubits, *Appl. Phys. Rev.* **6**, 021318 (2019).

- [S2] P.-R. Han, F. Wu, X.-J. Huang, H.-Z. Wu, C.-L. Zou, W. Yi, M. Zhang, H. Li, K. Xu, D. Zheng, H. Fan, J. Wen, Z.-B. Yang, and S.-B. Zheng, Exceptional entanglement phenomena: Non-hermiticity meeting nonclassicality, *Phys. Rev. Lett.* **131**, 260201 (2023).
- [S3] W. Tang, K. Ding, and G. Ma, Direct measurement of topological properties of an exceptional parabola, *Phys. Rev. Lett.* **127**, 034301 (2021).